The Background Properties of Suzaku/XIS

H. Yamaguchi[a], H. Nakajima[a], K. Koyama[a], T. G. Tsuru[a], H. Matsumoto[a], N. Tawa[b], H. Tsunemi[b], K. Hayashida[b], K. Torii[b], M. Namiki[b], H. Katayama[c], T. Dotani[c], M. Ozaki[c], H. Murakami[c], and E. Miller[d]

[a]Department of Physics, Graduate School of Science, Kyoto University, Kitashirakawa-Oiwake-cho Sakyo-ku, Kyoto 606-8502, Japan;
[b]Department of Earth and Space Science, Graduate School of Science, Osaka University, 1-1 Machikaneyama-cho, Toyonaka, Osaka 560-0043, Japan;
[c]The Institute of Space and Astronautical Science(ISAS) / Japan Aerospace Exploration Agency(JAXA) 3-1-1, Yoshinodai, Sagamihara, Kanagawa 229-8510, Japan;
[d]Center for Space Research, Massachusetts Institute of Technology(MIT), 77 Massachusetts Avenue Cambridge, MA 02139-4307, USA

ABSTRACT

Suzaku is the fifth Japanese X-ray astronomical satellite and it was launched in July 2005. The Suzaku X-ray Imaging Spectrometers (XISs) consist of four X-ray Charge-Coupled Device (CCD) cameras. Three of them are front-illuminated (FI) CCD, and the other is back-illuminated (BI) CCD. The strong points of the XIS are a high energy resolution, a large effective area, and a low and stable background. In particular, the background level of the Suzaku/XIS is much lower than the other X-ray satellites, XMM-Newton/EPIC and Chandra/ACIS. We investigated the background property of the XIS using the data obtained when the satellite is looking at the night earth, and proved the low level and the stability of the XIS background. Non X-ray background (NXB) consists of continuum component and some emission lines. The continuum component is very different between the FI-CCD and the BI-CCD. We discussed the positional dependence of the continuum component and the line components, and proved that the flux of the line components of the NXB is higher in the frame-store region than the imaging area. Finally, we investigated the effects of magnetic cut-off rigidity (COR) upon the count rate of NXB.

Keywords: X-ray telescope, Suzaku, CCD, XIS, Calibration, Background

1. INTRODUCTION

Suzaku was launched from Uchinoura Space Center (USC) on 10 July 2005 as the Japanese fifth X-ray astronomical satellite, and successfully put into the orbit. Unfortunately, the X-ray micro-calorimeter (X-Ray Spectrometer: XRS[1]), one of the main instruments of Suzaku, became not operational because of helium loss, but all of the other detectors, the Hard X-ray Detector (HXD[2]) and the X-ray Imaging Spectrometers (XISs), are still working properly. The HXD consists of phoswitch crystal scintillators (GSO/BGO) and PIN silicon solid-state detectors. Although the HXD has no imaging ability, it has a large energy range of 10–600 keV band, a narrow field of view (FOV) of $0.^\circ 56 \times 0.^\circ 56$ at < 100keV, and a good time resolution of 61 μsec. The sensitivity of the HXD is higher than any other hard X-ray detectors especially in the 10–200 keV band.

The XISs are composed of four sensors, and they are placed at the focal plane of four X-Ray Telescopes (XRTs[3]), which have a large effective area of 450 cm^2 at 1.5 keV per one telescope. Each sensor has a single Charge-Coupled Device (CCD) chip, which is a MOS-type three-phase CCD. Three of the CCD chips are the front-illuminated (FI) CCDs (XIS0, XIS2, XIS3), and the other is the back-illuminated (BI) CCD (XIS1).

All XISs are developed by the collaboration of Massachusetts Institute of Technology (MIT), Japan Aerospace Exploration Agency (JAXA)/Institute of Space and Astronautical Science (ISAS), Kyoto University, Osaka University, Rikkyo University, Ehime University, Kogakuin University, and RIKEN (The Institute of Physical and Chemical Research). We will describe the XISs in detail in the following section.

Further author information: (Send correspondence to H.Y.)
H.Y.: E-mail: hiroya@cr.scphys.kyoto-u.ac.jp, Telephone: +81 75 753 3869

Space Telescopes and Instrumentation II: Ultraviolet to Gamma Ray, edited by
Martin J. L. Turner, Günther Hasinger, Proc. of SPIE Vol. 6266, 626642, (2006)
0277-786X/06/$15 · doi: 10.1117/12.672183

2. DESCRIPTION OF THE XIS

2.1. Overview

The left panel of Figure 1 shows the schematic view of one XIS sensor. The hood is set up above the CCD to intercept X-rays and optical light from the outside of FOV. The optical blocking filter (OBF) is made of aluminum and polyimide film. The thicknesses of aluminum and polyimide are 0.12 μm and 0.1 μm, respectively. The OBF has a low transmission rate for optical light ($< 5 \times 10^{-5}$).

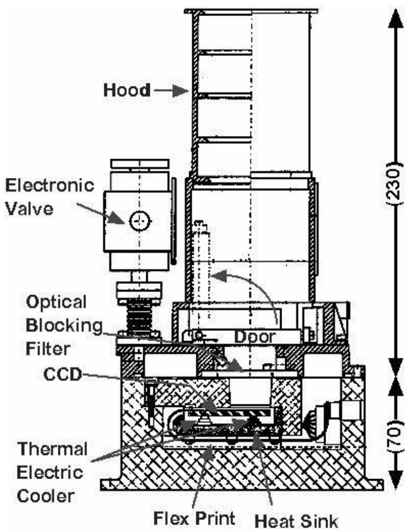

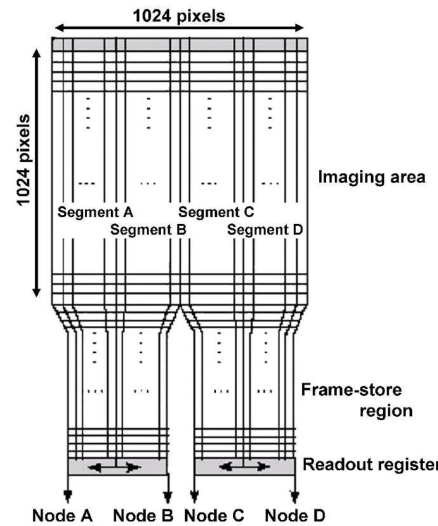

Figure 1. Left: Schematic view of the XIS camera. The single-hatched and cross-hatched regions are bonnet and base, respectively. Right: Schematic view of the CCD chip.

The CCD chip has an imaging area of 1024 $\times$ 1024 pixels and two frame-store regions of 512 $\times$ 1024 pixels, as shown in the right panel of Figure 1. The pixel size of imaging area and frame-store regions are 24 μm $\times$ 24 μm and 21 μm $\times$ 13.5 μm, respectively. The XIS has two CCD clock modes,[4] Normal mode and Parallel-sum (P-sum) mode. An exposure time and time resolution are determined according to the clock modes. The time resolution for the Normal mode is 8 sec which is the exposure time of imaging area per one frame, while, the time resolution for the P-sum mode is 7.8 msec. The chip has four readout nodes (Node A–D) and each node reads the signals from 256 columns of the chip, and then these divided regions of the chip are called as Segment A–D. Charges generated in the imaging area are simultaneously transfered to the frame-store regions, and read by the nodes in order. The time required to transfer one pixel is ~ 0.244 μsec. The field of view of the XIS is $\sim 18' \times 18'$. The CCD chip is cooled to -90 °C by the Thermo-Electric Cooler (TEC) which is controlled by the Thermal Controller Electronics (TCE). The analog signals from the sensor are transferred to the Analog Electronics (AE) and converted into the digital signals. Then they are sent to the Digital Electronics (DE) and X-ray events are extracted.

For on-orbit calibration, each sensor has ^{55}Fe calibration sources. Two sources are located on the side wall of the housing and illuminate two corners (top of the Segment A and D) of the imaging area. The image of the calibration sources is shown in Figure 2.

2.2. Performance

XISs consist of three FI CCDs and one BI CCD. Since there are no gate structure obstructing incident X-rays on the surface of the BI CCD, it has high quantum efficiency (QE) for soft X-rays. The left panel of Figure 3 shows the QE of the FI CCD and the BI CCD, which were modeled on the results of our ground calibration. We can see that the BI CCD has much higher QE below $\sim$4 keV than the FI CCD. However, because the depletion layer of the BI CCD is thinner than that of the FI CCDs (~ 75 μm and ~ 45 μm for the FI and the BI, respectively),

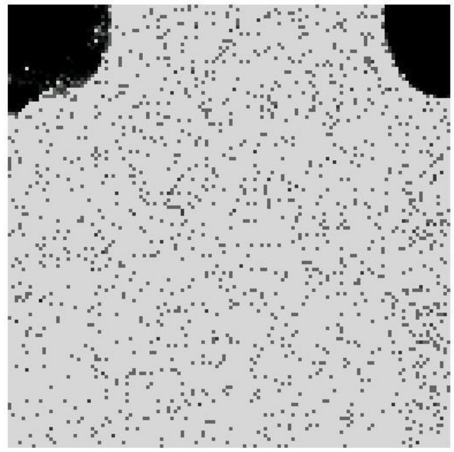

Figure 2. XIS2 image of the night earth data in 5.89 keV band. ^{55}Fe calibration sources illuminate two corners of the CCD chip.

the QE of the BI CCD for hard X-rays is lower than that of the FI CCDs. The FI CCDs have a neutral (non depletion) layer of $\sim$600 μm, while the BI CCD has almost no neutral layer. Since electrons generated in the neutral layer cannot be collected to the electrode, it spreads widely in the layer. The QE of the FI CCD and the BI CCD (before the launch) are 26% and 88% for 0.5 keV, 95% and 92% for 4.5 keV, and 57% and 39% for 8.5 keV, respectively.

Generally, the charge collection efficiency of BI CCDs is poorer than that of FI CCDs. Therefore the energy resolution of BI CCDs tends to become worse. For example, the energy resolution of the Advanced CCD Imaging Spectrometer (ACIS)-BI loaded into Chandra[5] was about two times worse than that of the FI devices, even before the launch. The XIS-BI is improved in this problem. By the chemisorption charging process,[6] the electric field between the surface and the electrode is strengthened. Then, the collection efficiency of photo-electrons is improved. We achieved very good energy resolution of the BI CCD comparable to the FI in the whole energy band of 0.2–13keV as shown in the right panel of Figure 3. The energy resolution of the FI and the BI are $\sim$130 eV at 5.9 keV before the launch.

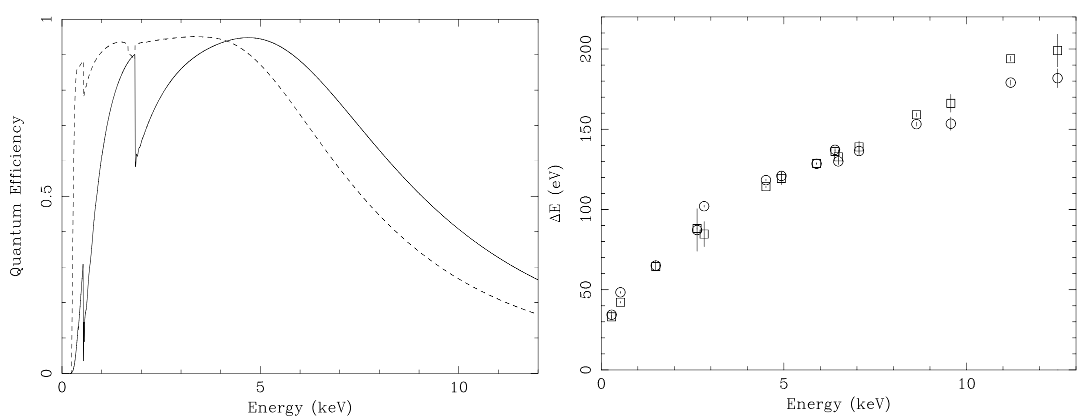

Figure 3. Left: Quantum efficiency of the FI CCD (solid line) and the BI CCD (dash line), which were modeled based on the results of the ground calibration. Right: Energy resolution of the FI CCD (square) and the BI CCD (circle), which were also the results of the ground calibration.

On the orbit, the QE and the energy resolution of the XIS are changing continuously. However we will not mention them here. Hayashida et al.[7] and Matsumoto et al.[8] refer to the problem in this issue.

2.3. Event Detection

We use the ASCA Grade method (see Figure 4) to detect X-ray events. In the case of the XIS, we consider that most of the X-ray events do not split into a region larger than 2×2 pixels, and we then regard the events of Grade 0, 2, 3, 4, and 6 as the X-ray events. On the other hand, all of the events which split over the 2×2 pixels region are classified into Grade 7 and regarded as background events, which are usually formed by the cosmic-ray.

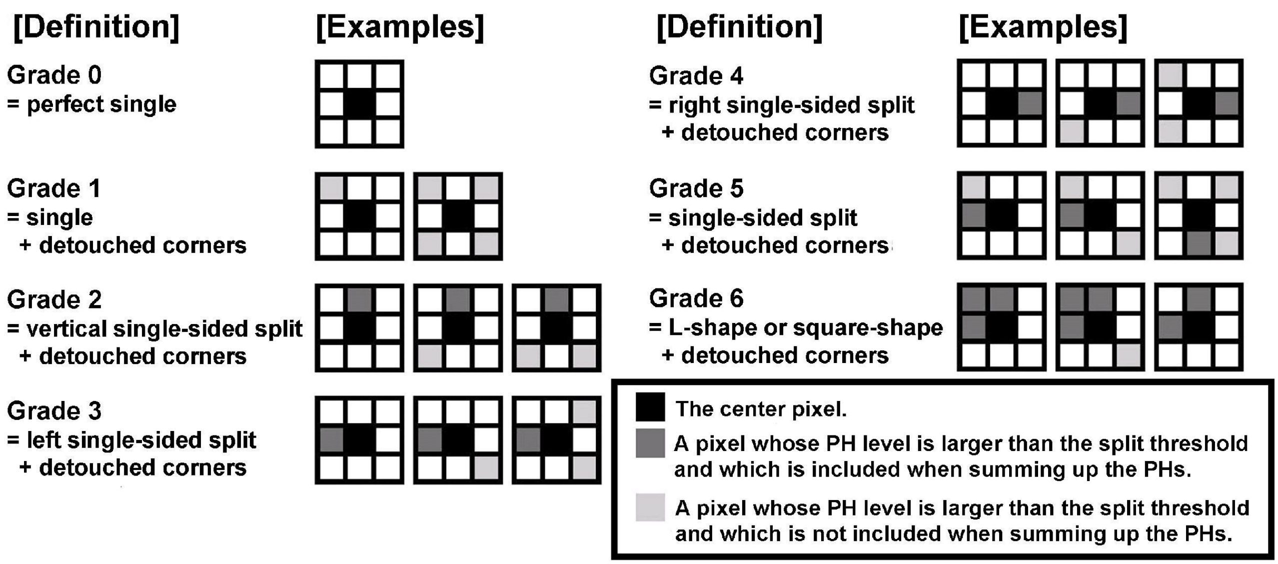

Figure 4. Classification of the ASCA Grade, which is also introduced in the XIS analysis. Grade 0, 2, 3, 4, and 6 are regarded as X-ray events.

3. BACKGROUND PROPERTIES

3.1. Background Components of The XIS

As shown in the previous section, the Suzaku/XIS has high efficiency and good energy resolution. In addition to them, the background level is also very important factor for X-ray detectors.

The background of the XIS mainly consists of the following components: (1)Non X-ray background (NXB), the origin of which is cosmic rays. The spectrum of the NXB has two components, a continuum and several emission lines. The continuum component is produced when the cosmic rays directly deposit their energy on the CCD chip, while the line components are produced by the interactions between the cosmic rays and the sensor housing. (2)Cosmic X-ray background (CXB), diffuse X-ray radiation coming from all directions of sky. The spectrum of the CXB corresponds to power-law spectrum of photon index of $\Gamma \sim 1.486$ for 1–20 keV band.[9] (3)Local Hot Bubble, diffuse X-rays from hot plasma surrounding the solar system. This component is dominant below $\sim$1 keV, and its intensity depends on the direction. Here, we discuss about the NXB only. The NXB spectra are available from the data when the satellite is looking at the dark side of the earth (night earth). We have continued to collect the night earth data since the beginning of the observation.

Figure 5 shows the FI spectra of the night earth and North Ecliptic Pole (NEP). The NEP spectrum includes the CXB and the local hot bubble components as well as the NXB, while the night earth spectrum consists of a pure NXB component. We can see that the NXB component is dominant above $\sim$6 keV for the XIS spectra.

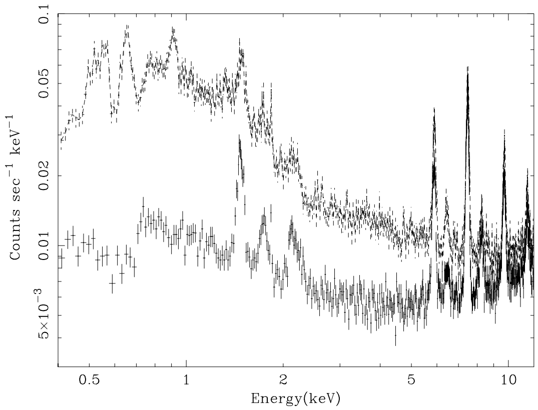

Figure 5. The night earth spectrum (solid) and the NEP spectrum (dashed) of the average of the three XIS-FI sensors.

Figure 6 compares the NXB spectra of each XIS sensor. The spectra are extracted from the whole region of the CCD chip, but the calibration source regions (see Figure 2) are excluded. Since the FI CCDs (XIS0, 2, 3) have the thick neutral layer as well as the thick depletion layer, most of the background events spread widely and are rejected as the Grade 7 events. On the other hand, the BI CCD (XIS1) has relatively thin depletion layer and almost no neutral layer, then relatively many background events remain. Therefore, the background count rate of the BI is higher than that of the FI, especially above ~7 keV. The spectra of the three FI sensors are quite similar, but only XIS0 has relatively strong Mn-K emission lines at 5.9 and 6.5 keV. The energy and count rates of the line components are shown in Table 1.

Table 1. Energy and count rate[a] of the line components of the NXB spectra.

Element	Transition	Energy [keV]	XIS0 10^{-9} [ct/s/pix]	XIS1 10^{-9} [ct/s/pix]	XIS2 10^{-9} [ct/s/pix]	XIS3 10^{-9} [ct/s/pix]
Al	Kα	1.486	$1.460^{+0.250}_{-0.250}$	$1.502^{+0.290}_{-0.290}$	$1.092^{+0.243}_{-0.243}$	$1.559^{+0.259}_{-0.259}$
Si	Kα	1.740	$0.421^{+0.179}_{-0.179}$	$1.612^{+0.274}_{-0.274}$	$0.262^{+0.175}_{-0.175}$	$0.581^{+0.196}_{-0.196}$
Au	Kα	2.123	$0.932^{+0.279}_{-0.279}$	$1.730^{+0.387}_{-0.387}$	$1.102^{+0.299}_{-0.299}$	$1.022^{+0.296}_{-0.296}$
Mn	Kα	5.895	$7.863^{+0.454}_{-0.454}$	$0.682^{+0.266}_{-0.266}$	$0.928^{+0.237}_{-0.237}$	$0.907^{+0.244}_{-0.244}$
	Kβ	6.490	$1.074^{+0.269}_{-0.269}$	0.000 (<0.284)	0.083 (<0.253)	0.085 (<0.309)
Ni	Kα	7.470	$5.253^{+0.389}_{-0.389}$	$4.824^{+0.443}_{-0.443}$	$5.813^{+0.406}_{-0.406}$	$5.953^{+0.409}_{-0.409}$
	Kβ	8.265	$0.681^{+0.236}_{-0.236}$	$0.644^{+0.500}_{-0.500}$	$1.005^{+0.249}_{-0.249}$	$1.451^{+0.253}_{-0.253}$
Au	Kα	9.671	$2.767^{+0.363}_{-0.363}$	$5.143^{+0.747}_{-0.747}$	$3.197^{+0.384}_{-0.384}$	$3.010^{+0.375}_{-0.375}$
	Kβ	11.51	$1.395^{+0.384}_{-0.384}$	$1.808^{+1.052}_{-1.052}$	$1.585^{+0.411}_{-0.411}$	$1.727^{+0.383}_{-0.383}$

[a] The calibration source regions are excluded.

3.2. Comparison with Other Satellites

Although Chandra has very high spatial resolution, its effective area is much smaller than Suzaku. On the other hand, XMM-Newton has large effective area, and good energy resolution comparable to the Suzaku/XIS. Therefore, we will compare in detail the performance of the Suzaku/XIS with the XMM-Newton/EPIC in this section. Table 2 shows the comparison of spatial resolutions and effective areas between Suzaku and XMM-Newton. The total effective area of XMM-Newton is larger than that of Suzaku. In the spectral and imaging analysis, however, not only the effective area but the signal/noise (S/N) ratio is essentially important. We compare the NXB spectra of Suzaku and XMM-Newton, and investigate the S/N ratio of their observations. The NXB spectra of XMM-Newton are extracted from "CLOSED" data which were taken with the filter wheel

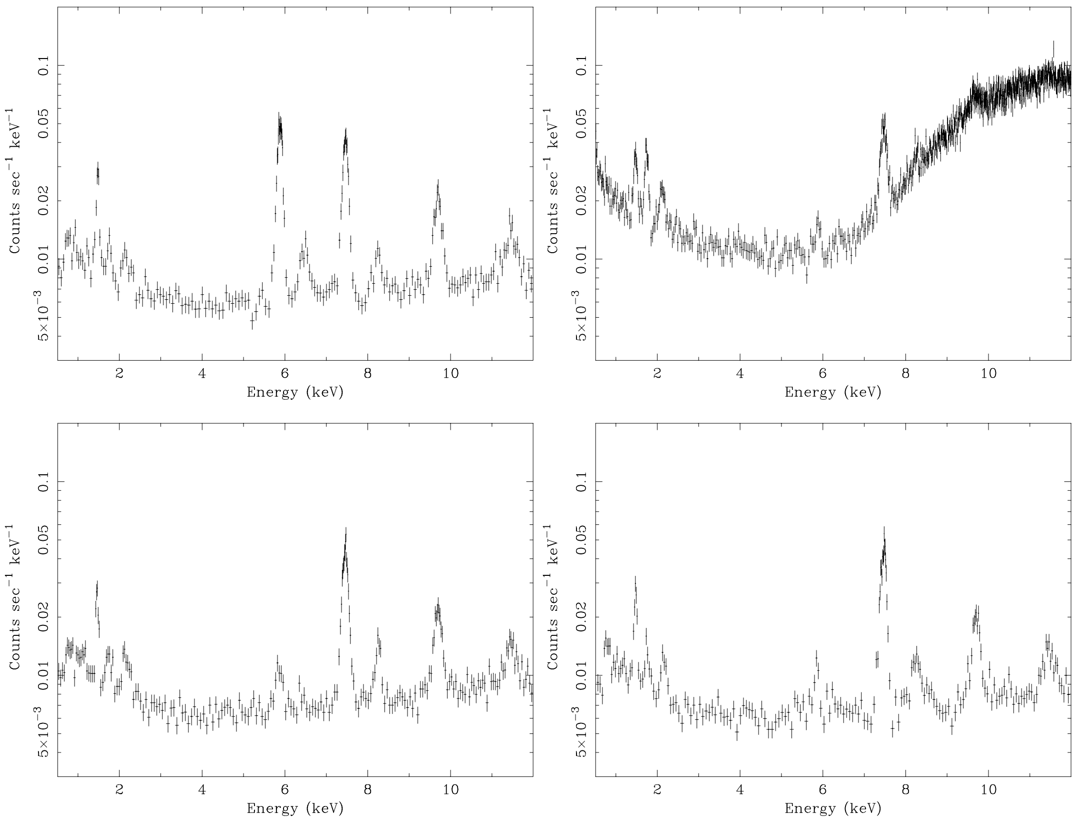

Figure 6. The NXB spectra of XIS0 (top-left), XIS1 (top-right), XIS2 (bottom-left), and XIS3 (bottom-right).

in the closed position. Figure 7 shows the background spectra of Suzaku and XMM-Newton normalized by the solid angle of the FOV and by the effective area. Therefore, it represents the surface brightness of the background, and gives a measure of the S/N ratio for diffuse objects. The background level of the EPIC-MOS is ∼5 times higher than that of the XIS-FI and is comparable to that of the XIS-BI above ∼6 keV, where the NXB component is dominant in the background spectra. The background continuum level of the EPIC-pn is lower than that of EPIC-MOS, however the spectrum of the XMM/pn has very strong emission lines (Ni, Cu, Zn) above 7 keV. The intensity of Al-Kα line at 1.49 keV of the Suzaku/XIS is also much weaker than that of the XMM-Newton/EPIC. Therefore, it is proved that the Suzaku/XIS-FI has the lowest background level (the highest S/N ratio) for diffuse objects. Furthermore, the XMM background frequently shows “background flare”, and the background count rate varies by a factor of about 100. Since the orbit altitude of Suzaku is much lower than XMM-Newton and Chandra, Suzaku is less influenced by solar flares, and then the background level of Suzaku is very stable (see Figure 8). Therefore, the Suzaku/XIS is very sensitive to diffuse dim sources especially in the hard X-ray band.

3.3. Positional Dependencies

The background events of the XIS have spatial variations. The left panel of Figure 9 shows that the NXB count rate depends on “ACTY”. Actual (ACTX, ACTY) coordinates define the actual pixel position on the CCD imaging area. The pixel of Segment A in the imaging area which is the nearest to the readout node is defined as (ACTX,ACTY) = (0,0), and the ACTY axis is in the direction opposite to the parallel charge transfer. Therefore, ACTY corresponds to the number of parallel transfer in the imaging area. As shown in the left panel of Figure 9, the NXB count rate increases gradually with ACTY. Charges generated in all pixels of the imaging area are transferred to the frame-store region all at once. This transfer is called “frame-store transfer” and requires the

Table 2. Spatial resolutions and effective areas of Suzaku and XMM-Newton.[10]

Instrument	HPD[a]	EA[b] @1keV [cm^2]	EA[b] @8keV [cm^2]
Suzaku XIS-FI	$1.8'$[c]	220[c]	150[c]
Suzaku XIS-BI	$2.4'$	320	100
XMM EPIC-MOS	$14''$	400	100
XMM EPIC-pn	$15''$	1200	600

[a] Half Power Diameters.

[b] Effective areas with detector responses (per one unit).

[c] Value for XIS0

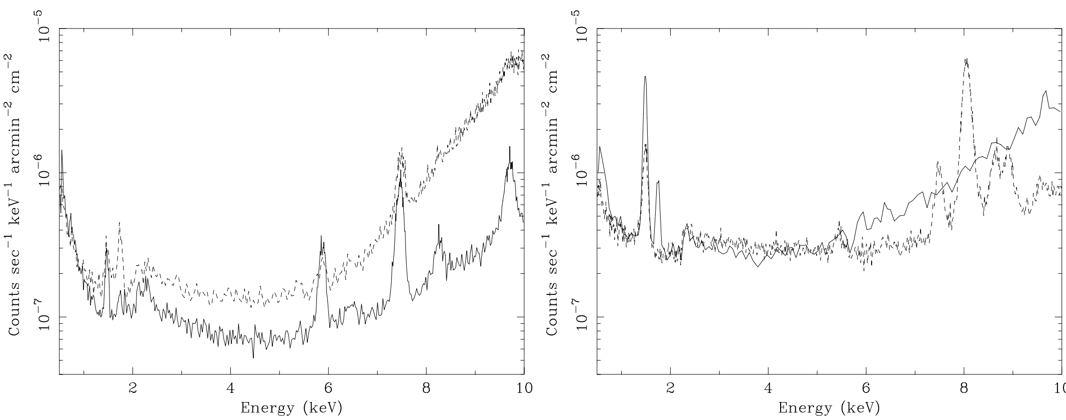

Figure 7. Comparison of the NXB spectra normalized by the solid angle of the FOV and by the effective area between the Suzaku/XIS and the XMM/EPIC. Left: XIS-FI (solid) and XIS-BI (dashed). Right: EPIC-MOS (solid) and EPIC-pn (dashed).

transferring time of ∼25 msec. Then, the charges stored in the frame-store region are transferred and read out one by one, and ∼6.925 sec is required to reading out of all charges. Therefore, the events detected in ACTY=0 are immediately read out after the frame-store transfer, while the events detected in ACTY=1023 are transfered slowly in the frame-store region and read out 6.925 sec after the frame-store transfer. The frame-store region is shielded from X-ray and optical light, but the NXB events are still detected in this region. Therefore, we can consider that the count rate dependency on ACTY is due to background events detected in the frame-store region.

The right panel of Figure 9 shows the same dependencies to the left panel, but counts at each ACTY region are normalized by counts at ACTY=0. Here, we define the counts at ACTY as C(ACTY). We can measure the NXB intensity ratio of the the frame-store region to the imaging area by the slopes of these plots. Although all NXB components have similar correlation, the slopes are different between the continuum component and the line components. The slope for the continuum component (3–7 keV), the Al line (1.49 keV), and the Ni line (7.47 keV) are 3.2×10^{-4}, 5.3×10^{-4}, and 5.2×10^{-4}, respectively. Since the exposure time of the imaging area is 8 sec, C(0)/8 corresponds to the count rate of the NXB events detected in the imaging area. While, [C(1023)-C(0)]/6.925 can be considered as the count rate of the NXB events detected in the frame-store region. Then,

$$R = \frac{\mathrm{C}(1023) - \mathrm{C}(0)}{6.925} \div \frac{\mathrm{C}(0)}{8}$$

is equal to the NXB intensity ratio of the the frame-store region to the imaging area, and R for the continuum component, the Al line, and the Ni line are calculated to 0.37, 0.61, and 0.60, respectively. The ratio of the pixel size of the frame-store region to that of the imaging area is ∼0.49 (see Section 2.1). If the "flux" of the NXB is

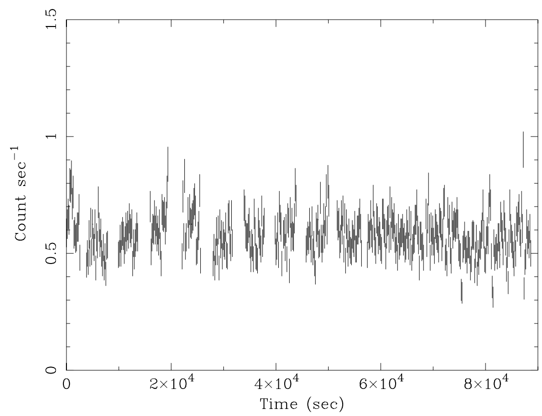

Figure 8. XIS2 light curve above 10 keV, which is obtained from the observation of NEP.

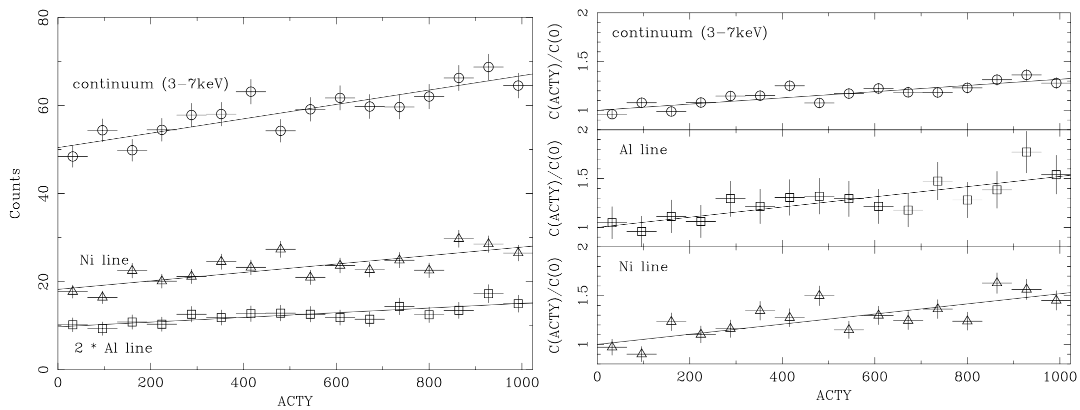

Figure 9. Left: The count numbers of the continuum component in 3–7 keV band (circle), twice of Al line (square), and Ni line (triangle) as the function of ACTY. The solid lines show the best fit model fitted with linear function. All data are extracted from the night earth data of XIS2. Right: The same correlation to the left panel, but the count numbers of each ACTY region are normalized by the counts of ACTY=0.

uniform in the imaging area and the frame-store region, it is natural that the value of R is lower than 0.49 like the value for continuum component, because the fraction of the Grade 7 events (rejected in the event detection process) increases when the pixel size is smaller. However, the values of R for the line components (both Al and Ni) are higher than 0.49. This result suggests that the flux of the NXB line components is higher in the frame-store region than the imaging area.

In addition to the dependency on ACTY, we discovered the positional dependencies which are proper to each sensor. As the spectra shown in Figure 6, the Mn-K line is intense only in the XIS0 spectrum, and this component shows the non-uniform spatial distribution shown in the left panel of Figure 10. The origin of this component is possible to be scattered X-rays from the calibration sources which illuminate two corners of the imaging area, or direct X-rays from the ^{55}Fe source which stick on the CCD chip or housing. In order to determine the origin, we extracted the spectra from the calibration source regions and the non-uniform component region, and compared the intensity ratio of Mn-Kβ to Mn-Kα of each region. Then, the intensity ratio of the calibration sources regions and the non-uniform component region are calculated to be $\sim$ 0.33, and $\sim$ 0.13, respectively. If the origin of the non-uniform component is the scattered X-rays, the intensity ratio of this region should be consistent with that of the calibration sources regions. Furthermore, the intrinsic intensity ratio of Mn-Kβ to Mn-Kα from ^{55}Fe sources is $\sim$ 0.1, which is comparable to the ratio for the non-uniform component. On the other hand, the calibration sources of the XIS are covered with filters whose transmission rate for Mn-Kα is lower than that for Mn-Kβ, therefore the intensity ratio for the calibration sources becomes relatively high. Therefore, this result suggests that the origin of the non-uniform Mn-K line component is the direct X-rays from the sticking ^{55}Fe source. However, the reason why such source stuck is still unknown.

The Si-K line component also has the non-uniform spatial distribution. The right panel of Figure 10 shows the XIS2 image in the 1.74 keV band. Since Si line is intense near the calibration sources regions, we can consider that the Si line events are mainly due to the escape events of the X-rays from the calibration sources.

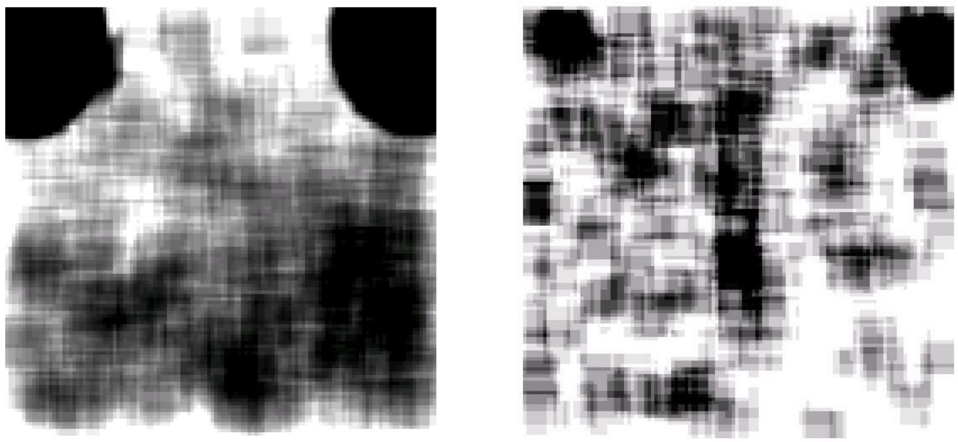

Figure 10. Left: XIS0 image of the night earth data in 5.89 keV (Mn-Kα) band. Right: XIS2 image of the night earth data in 1.74 keV (Si-Kα) band.

3.4. Dependency on Cut-off Rigidity

The count rate of the NXB has a dependency on the magnetic cut-off rigidity (COR). Figure 11 shows the NXB spectra extracted from the different COR regions. The count rate of the NXB increases as the COR decreases.

In order to subtract the background from target observation data accurately, the COR effect for the NXB spectrum should be considered. We prepared the night earth spectra of each COR region. A COR weighted background spectrum for each observation can be constructed by using these night earth spectra.

SUMMARY

Using the XIS night earth data, we studied the background property of the XIS. We proved that the NXB level of the XIS-FI is lower and more stable than the other satellites. We investigated the spatial variations of the NXB events of the XIS, and proved the flux of the line components of the NXB events is higher in the frame-store region than the imaging area. We showed the count rate of the NXB has a dependency on the COR. XIS calibration team provided the NXB spectra of each COR region for accurate background subtraction from the observation data of the XIS.

ACKNOWLEDGMENTS

We thank all of the members of the XIS team and the Suzaku science working group. H. Y. and H. N. are supported by Japan Society for the Promotion of Science (JSPS) Research Fellowship for Young Scientist.

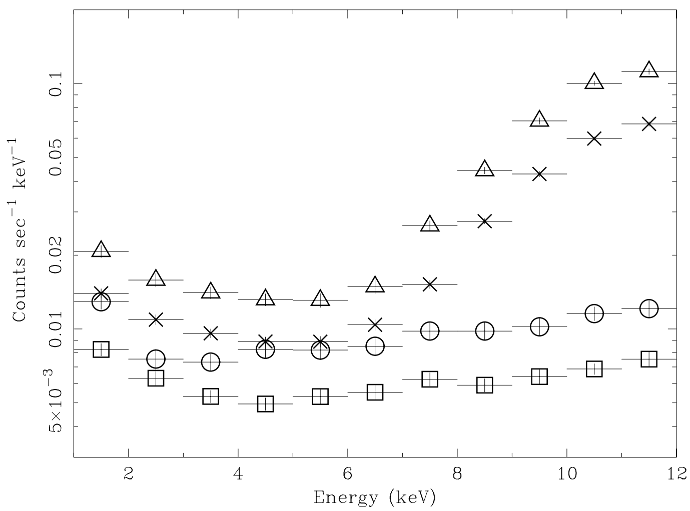

Figure 11. The NXB spectra of XIS2 (FI) in the COR region of below 10 GeV/c (circle), and above 10 GeV/c (square), and that of XIS1 (BI) in the COR region of below 10 GeV/c (triangle), and above 10 GeV/c (cross).

REFERENCES

1. K. Mitsuda, et al., ASP Conf. Ser. 251, 570, 2001
2. Y. Fukazawa, et al., Proc. SPIE, (this issue)
3. K. Misaki, et al., Proc. SPIE, 4851, 459, 2004
4. H. Matsumoto, et al., NIM A, 541, 357, 2005
5. M. C. Weisskopf, et al., Publ. Astron. Soc. Pacific 114, 1, 2002.
6. B. E.Burke, et al., IEEE Trans. ED-46, 1069, 1991
7. K. Hayashida, et al., Proc. SPIE, (this issue)
8. H. Matsumoto, et al., Proc. SPIE, (this issue)
9. Y. Ishisaki, et al., PhD Thesis, The University of Tokyo, 1996
10. H. Feng, et al., A&A 402, 1151, 2003